Mechanisms for dynamic crack branching in brittle elastic solids: Strain field kinematics and reflected surface waves

T. Martín,[1,2] P. Español,[1] and M. A. Rubio[1]
[1]*Departamento Física Fundamental, Facultad Ciencias, Universidad Nacional de Educación a Distancia, Senda del Rey 9, Madrid-28040, Spain*
[2]*Departamento Ciencias Básicas Aplicadas a la Ingeniería Forestal, E.U.I.T. Forestal, Universidad Politécnica de Madrid, Ciudad Universitaria, Madrid-28040, Spain*
(Received 29 July 2004; published 8 March 2005)

We report on a numerical simulation study of dynamic fracture in strip-shaped plates in which we implement a fracture criterion that fully respects mode-I symmetry. The crack dynamics is studied as a function of the length of the initial notch. The cracks show accelerated straight motion until branching appears. We show that branching can be triggered by two different mechanisms: namely, the kinematics of the strain field and back-reflected surface waves traveling on the crack lip. We also propose a qualitative explanation for the kinematic branching mechanism in terms of the effects of the lattice discretization on Yoffe's stress field. The kinematic branching mechanism is understood by analyzing the disconnection times of the nodes ahead and aside of the crack tip.

DOI: 10.1103/PhysRevE.71.036202 PACS number(s): 05.45.Pq, 62.20.Mk, 46.50.+a, 02.70.Ns

I. INTRODUCTION

The understanding of how materials break apart under external loads is a subject that has attracted the attention of scientists and engineers for a long time. The problem has obvious relevance from a technological (resistance of materials and safety) as well as environmental (earthquake activity and seismic hazard) points of view. From a physical perspective, this problem is interesting because of the complexity of its dynamics, in which singularities appear and many different length and time scales are involved. Furthermore, the complex fracture patterns that may appear in experiments have strong resemblances with other pattern formation processes much studied, such as diffusion limited aggregation [1], dielectric breakdown [2], and percolation [3,4].

Different fracture mechanisms may appear depending on some features of the materials. A first classification separates materials into two classes according to the predominant fracture mechanism. Brittle materials behave as elastic solids until the fracture threshold is reached. Ductile materials show plastic deformation, and dislocation motion plays an essential role in the dynamics. In this paper we will focus on brittle fracture dynamics.

Linear elastic fracture mechanics [5,6] assumes that at the tip of the crack there is a stress singularity with a radial dependence such as $1/\sqrt{r}$. This singularity is characterized by a coefficient named the stress intensity factor, which, for obvious safety reasons, has been the main concern in engineering fracture mechanics. From this point of view, modern numerical techniques that include a properly implemented cohesive zone at the crack tip give satisfactory predictions about stress intensity factors [7].

In the last quarter of the 20th century modern experimental and computational equipment made dynamic fracture a suitable subject of study (for an extensive review of experimental results see, for instance, Ref. [8]). In a series of papers Ravi-Chandar and Knauss [9] studied the relationship between crack tip speed and the surface roughness at the crack lip, stating the well-known classification of mirror, midst, and hackled zones according to the amplitude of the surface irregularities. More recently, extensive experimental work on glass and PMMA [8] has shown the important role that mechanisms such as acoustic emission [10–12], wave reflection [13], and branching [14] may have on the dynamical behavior of cracks.

From a dynamical perspective, however, many aspects concerning crack motion are still the subject of debate, and some of the open questions concern the mechanisms limiting the speed of a moving crack. According to the theoretical predictions for brittle linear elastic solids, the speed of a crack tip in straight motion should be ruled by the balance between the elastic energy flow towards the crack tip and the energy dissipated in creating crack lip surface. Under this assumption, the maximum speed in straight crack motion should be the Rayleigh surface wave speed V_R [5,6]. Nevertheless, the experimental studies of crack propagation show a rich and complex phenomenology. Regarding experiments carried out with PMMA (a material that shows brittle behavior) it has been found that there are no fractures propagating at a velocity lower than $0.18V_R$ or higher than $0.7V_R$ [10,12]. Moreover, when the crack speed exceeds a critical value of about $\approx 0.4V_R$, oscillations of the tip speed appear and acoustic emission takes place [11].

Acoustic emission [10–12] and branching [14] have been proposed as mechanisms limiting the crack tip velocity. Wave emission has been recently studied in two different discrete models [15,16]. Their results show that at low crack speeds surface wave radiation dominates, while at high crack speed bulk wave radiation does [15], and that surface wave radiation can be a very efficient energy dissipation mechanism at speeds in which resonance occurs [16].

Furthermore, even the mechanism causing branching is not fully clear. Most of the discussion about the branching

mechanism starts from Yoffe's asymptotic solution for the stress field around a moving crack [17]. Yoffe's solution allows for different qualitative interpretations of branching [5,6], based on either the lateral maximum that develops in the angular dependence of the hoop stress or the changes in the angular dependence of the highest eigenvalue of the stress tensor at the crack tip [18]. To our knowledge there are no conclusive data from either experiments or simulations that favor any of these interpretations.

Moreover, the value of the branching angle seen in experiments, which is typically in the range between 10° and 20° [8], cannot be explained on the basis of Yoffe's asymptotic solution. Only recently have there been some predictions of the value of the branching angle under general loading conditions [19].

From a theoretical point of view, the coupling of the equations of linear elasticity and the boundary conditions, together with the singularity present at the crack tip, makes the problem quite difficult to treat. In spite of the difficulty of the problem, many theoretical results have been achieved mostly related to static or straight advancing cracks. However, dynamic cracks with complex patterns are still far away from the current state of theoretical work. In this sense, numerical simulations offer a way to get some insight into the complex features of fracture dynamics without solving analytically the whole problem. Many different simulation schemes have been proposed, and a good account of different approaches can be found in Ref. [20]. Large multiscale molecular dynamics simulations [21,22] can be implemented in nowadays top-level computing facilities. Suitable medium-scale lattice simulations [16,23–27] are still useful in order to study dynamic fracture from a fundamental point of view, though.

In numerical simulations of dynamic fracture, apart from specifying the force law that acts between material points, it is necessary to decide when a portion of material will break apart; that is, one essential ingredient of the problem is the so-called *fracture criterion*. Many fracture criteria have been proposed in the literature, most of them relying on some form of bond cutting scheme. This poses an additional problem because the singularity being at the tip, the superposed effect of the lattice topology right at the tip, and the way the bond cutting is implemented can dramatically affect the dynamics of the crack. This has been shown most clearly in our previous work [25] in which we demonstrated that an asymmetry in the crack tip induced by the bond cutting procedure creates an important mode-II component in a plate configuration that was supposedly formulated for mode-I loading.

The purpose of the present paper is threefold: first, to propose a fracture criterion that, in the same conditions stated in our previous paper [25], yields a fully symmetric mode-I loading (basically, the fracture criterion is as follows: one lattice node will be disconnected from its neighbors if the maximum eigenvalue of the strain tensor at this node overcomes a certain threshold value), second, to study the changes in fracture pattern and dynamics depending on the length of the notch practiced on the plate, and third, to present a study of the branching instabilities appearing in the simulations. In this aspect, we show that two different branching instabilities may occur: one of them can be explained in terms of the kinematics of the strain tensor field of a Yoffe solution in a discrete medium; the other is induced by the arrival at the crack tip of a surface wave pulse, generated at the moment that crack motion starts, after being reflected at the upper boundary of the plate.

This paper is organized as follows: in Sec. II we present a brief overview of the discretization method of the elastic wave equations as well as a description of the fracture criterion and the simulation procedure. In Sec. III we report the simulation results concerning the static strain field and its dependence on notch length. In Sec. IV we show a detailed study of the fracture dynamics, including pattern structures, kinematics, and branching phenomena. In Sec. V we propose a qualitative explanation of the branching mechanism based on the kinematics of the strain tensor. Finally, a discussion of the results and conclusions are presented in Secs. VI and VII, respectively, including some proposals for future work.

II. MODEL AND GENERAL METHODOLOGY

The discretization method has been fully described in Ref. [25]. For the sake of completeness we briefly outline here the general framework and the final formulation of the simulated equations. The equations of elasticity that govern the displacement field $\mathbf{u}(\mathbf{r},t)$ in a homogeneous linear material subject to small deformations are [5]

$$\ddot{\mathbf{u}}(\mathbf{r},t) = c_\perp^2 \nabla^2 \mathbf{u}(\mathbf{r},t) + (c_\parallel^2 - c_\perp^2)\, \boldsymbol{\nabla}\, (\boldsymbol{\nabla} \cdot \mathbf{u})(\mathbf{r},t), \tag{1}$$

where the transverse $c_\perp$ and longitudinal $c_\parallel$ sound speeds are material properties related to Young's modulus E and Poisson's coefficient ν. In the case of plane strain, as corresponds to the situations here considered, the expressions of the transverse and longitudinal wave speeds are, respectively,

$$c_\perp = \left(\frac{E}{2\rho(1+\nu)} \right)^{1/2},$$

$$c_\parallel = \left(\frac{E(1-\nu)}{\rho(1+\nu)(1-2\nu)} \right)^{1/2}, \tag{2}$$

where ρ is the mass density of the material. For the purposes of this study the Rayleigh surface wave speed may be approximated by the expression [28]

$$V_R \approx c_\perp (0.874 + 0.162\nu). \tag{3}$$

On the other hand, the discretization method reported in Ref. [25] yields the following expression, for the case of a triangular lattice:

$$\ddot{\mathbf{u}}_i(t) = \left[\frac{c_\perp^2 - c_\parallel^2/3}{a^2} \right] \sum_{j=1}^{6} (\mathbf{u}_j - \mathbf{u}_i) + \frac{4(c_\parallel^2 - c_\perp^2)}{3a^2} \times \sum_{j=1}^{6} (\mathbf{u}_j - \mathbf{u}_i) \cdot \hat{\mathbf{r}}_{ji}^0 \hat{\mathbf{r}}_{ji}^0, \tag{4}$$

where a is the lattice spacing and $\hat{\mathbf{r}}_{ji}^0$ is the undeformed lattice vector joining particles j and i. These equations can be interpreted as the equations of motion for a set of portions of material of unit mass in a lattice, interacting with their nearest neighbors with a linear law of force. The main advantage

of this formulation is that it allows for a numerical simulation to be implemented by means of molecular dynamics algorithms.

It is worth noting that the above discrete model coincides with the Born model [29], usually characterized by the potential energy

$$V = \frac{1}{2}\beta \sum_{ij} [\mathbf{u}_i - \mathbf{u}_j]^2 + \frac{1}{2}(\alpha - \beta) \sum_{ij} [(\mathbf{u}_i - \mathbf{u}_j) \cdot \hat{\mathbf{r}}_{ji}^0]^2, \quad (5)$$

where α, β are model constants. Consequently, the force on particle i is given by

$$\mathbf{F}_i = -\frac{\partial V}{\partial \mathbf{u}_i} = \beta \sum_{ij} (\mathbf{u}_j - \mathbf{u}_i) + (\alpha - \beta) \sum_{j} (\mathbf{u}_j - \mathbf{u}_i) \cdot \hat{\mathbf{r}}_{ji}^0 \hat{\mathbf{r}}_{ji}^0. \quad (6)$$

It can be seen that both expressions of the force law have the same two terms, the first one being a restoring force and the second an anharmonic term. This resemblance allows for a determination of the constants α and β of the Born model in terms of the material properties.

The strain tensor is defined as $\gamma = \frac{1}{2}[\nabla u + \nabla u^T]$. This expression can be readily translated to the discretized lattice, and one obtains for the strain tensor defined at each lattice node

$$\gamma_i = \frac{1}{6a} \sum_j (\mathbf{u}_i - \mathbf{u}_j) \hat{\mathbf{r}}_{ji}^0 + \hat{\mathbf{r}}_{ji}^0 (\mathbf{u}_i - \mathbf{u}_j). \quad (7)$$

For latter reference, a direct translation of the continuum formula to this case yields the expression of the stress tensor σ_i at the node i in terms of the strain tensor according to [28]

$$\sigma_i = \frac{E}{1+\nu} \left(\gamma_i + \frac{\nu}{1-2\nu} \mathrm{tr}\ \gamma_i \mathbf{1} \right). \quad (8)$$

As the strain tensor is the primary result of the simulation, the whole discussion of the results reported in this paper has been made of the strain tensor.

A last comment on the discrete model is in order here: as stated in Ref. [25], the discretization here presented is equivalent to a first-order finite-difference spatial scheme; hence, the stability of the algorithm depends on the actual parameter values. In this case, the scheme is unstable for $\nu > 0.25$; this particular value of the Poisson's coefficient is the one at which the coefficient of the linear spring force in Eq. (4) changes sign. This problem can be eliminated by reformulating the model by considering also the next-nearest-neighbor interaction [30].

A. Fracture criterion

The fracture criterion is a crucial ingredient for the simulations of crack dynamics. The simplest physical representation of the breaking process is that the interaction between two points of the material will vanish if they are tonn apart more than a given threshold distance. This is usually implemented in terms of a *most-stretched bond rule*. In dynamic crack simulations, this is readily carried out by setting a given strain threshold; therefore, the bond that will overcome that threshold will break. This criterion has been implemented, for instance, in Refs. [25,27] and others.

However, the use of this criterion shows local effects, such as lattice trapping or an alternating mode-II perturbation [25], making it difficult to analyze the shape and dynamics of the tensor fields obtained from the simulations [25,27]. Moreover, in simulations where the strain is imposed normal to one of the triangular lattice directions, oblique branches always leave unbroken bonds parallel to the unstrained lattice direction.

For those reasons, we propose a different fracture criterion implemented not on the bonds connecting two portions of material, but on the nodes themselves. The formulation of the criterion is as follows: when the maximum eigenvalue of the strain tensor at a mesh node, γ_i^+, exceeds a given threshold value γ_c^+, the interaction between the node and its neighbors is assumed to vanish, and the crack propagates through the "void" created. This criterion closely resembles the one used in Ref. [16] or those based on "phase field" descriptions [26].

This formulation of the fracture criterion has several advantages. First, it fully respects the symmetry with respect to the crack line, in straight propagating cracks. Therefore, the simulations here presented are completely free of the alternating mode-II perturbations that appeared in our previous work [25]. Second, as we will later highlight, it considerably decreases lattice trapping. No unbroken bonds are left in oblique branches. Finally, working with the strain tensor instead of the stress tensor makes unnecessary additional assumptions on the relationship between the deformation tensor and the stress tensor for the material described by the discretized equations.

B. Simulation procedure

Equation (4) has been simulated with a conventional molecular dynamics code using Verlet's algorithm (i.e., a centered difference in time) [31]. This is an explicit method in the terminology of finite-difference simulations. The units chosen are the lattice spacing a for spatial coordinates and the Rayleigh wave speed V_R for velocities. Consequently, the time unit is a/V_R.

We have studied mode-I fracture of finite two-dimensional (2D) rectangular plates of dimensions $L_x \times L_y$ containing an initial sharp notch of length L_n that can be adjusted at will. The notch is located in the middle of the plate and is made by cutting n transversal bonds in the two central columns starting from the upper boundary (see Fig. 1). Note that the selected configuration is, therefore, fully symmetric with respect to the middle vertical plane, and, consequently, if properly simulated, the dynamics should be free of any mode-II perturbations.

For further reference we also show the detailed structure of the nodes close to the tip in Fig. 2, where we have labeled the nodes close to the tip in the following way: P_0 is the node that was last "disconnected," P_1 is the node that should be next disconnected if straight propagation occurs, and P_2 are both the two lateral nodes that should be disconnected if branching occurs.

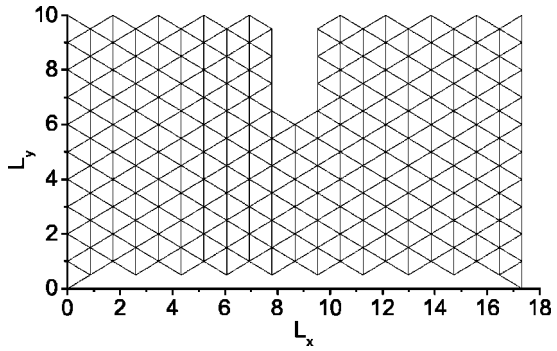

FIG. 1. Triangular lattice with a symmetric notch located in the middle of the plate, beginning from the upper free boundary. The dimensions of the plate shown are $L_x=17.3$, $L_y=10$. The length unit is the lattice spacing a.

Typically, plates of 80 000 nodes are studied. The plate is subject to a mode-I deformation by displacing the nodes of the right wall a fixed distance ΔL_x in the x direction. The plate is left to equilibrate until the stationary stress field corresponding to the given geometry is reached. During this equilibration time, a damping force is applied to each node in order to speed up the equilibration process and get rid of all of the waves excited due to the application of the deformation. The equilibration time is several times longer that the time required by sound waves to travel back and forth through the plate. The evolution of the equilibration process was monitored through the evolution of the highest eigenvalue of the strain tensor at the notch tip, γ_0^+. The plate was considered to be in equilibrium when the time variation of γ_0^+ was smaller than ± 0.001 in the selected units. In this way, we are starting the simulation with all nodes at rest effectively reproducing the experimental conditions of quasiestatic loading before fracture initiation.

The simulations have been performed at a given nominal deformation $\epsilon=0.01$. We have adjusted the critical strain by computing the strain tensor at each mesh node. Once the notch is "cut" and the plate is equilibrated, we compute, at each node, the eigenvalues of the strain tensor, which we label γ_i^+ and γ_i^-. Then we find the node i, which has the highest value of γ_i^+, and this value is set as γ_c^+; in all cases, the node with the highest γ_i^+ was the node at the tip of the notch, so that $\gamma_c^+=\gamma_0^+(t=0)$. When the equilibration process is finished and the breaking strain threshold γ_c^+ is set equal to $\gamma_0^+(t=0)$, the crack starts propagating. During the simulations, the nodes that went above threshold were "disconnected" from their neighbors by removing them from the Verlet's neighbor list [31]. Note that this implementation precludes the possibility of surface recombination [32].

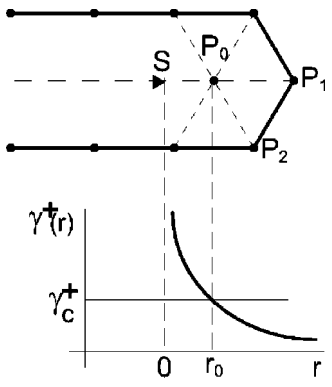

FIG. 2. Detailed structure close to the crack tip. S is the effective position of the singularity, P_0 is the last disconnected node, P_1 if the next node to be disconnected if straight propagation occurs, and P_2 are the nodes to be disconnected if branching occurs.

The time step had to be adjusted depending on the spatial resolution of the simulation. The procedure used to adjust the time step was to perform a series of simulations at a given spatial resolution and to diminish the time step until no change in the crack dynamics, both including kinematics and fracture patterns, occurred. In all of the simulations reported in this work the time step was $\delta t=0.002$ for plates with $L_x=100\sqrt{3}$ and $L_y=400$ (in the selected units). The Poisson coefficient has been set to a value $\nu=0.25$, so that the corresponding values of the transversal and longitudinal wave speeds are $c_\perp=1.0935$ and $c_\parallel=1.894$, respectively (the Rayleigh wave speed is $V_R=1$). Some other simulations have been carried out with different values of ν, in particular with $\nu=0.2$; the dynamics observed is similar to that presented in this paper.

The simulations of the crack dynamics start when γ_c^+ is set equal to $\gamma_0^+(t=0)$. Then the node at the notch tip, P_0, is "disconnected" at the first time step, and the subsequent evolution of the strain field as well as the wave propagation along the crack edge makes the crack to advance.

III. STATICS

We have conducted a series of simulations in which the effect of L_n on the dynamics of crack propagation is studied systematically. The notch length determines the level of stress of the landscape on which the crack propagates and it is usually the way in which this effect is investigated experimentally.

In Fig. 1 we show a plate in which the lattice is oriented with a lattice direction along the vertical axis; the notch is also oriented in the direction of the vertical axis, and the plate is strained in the direction of the horizontal axis.

The dependence of γ_c^+ on L_n is shown in Fig. 3. Open symbols represent the actual value of γ_c^+ obtained directly after the equilibration process, at each value of L_n. Figure 3 shows a strong increase of γ_c^+ at short notch length and a saturation for long notches at a value that we label γ_{sat}. These results can be cast in a different way that allows for closer comparison with experiments: in experiments carried out with plates made of the same material, one may expect that γ_c^+ should be a property of the material and, therefore, independent of L_n. Hence, one may think in terms of the equivalent strain ϵ_{eq} that should be imposed externally for plates with different initial notches to break at the same value of γ_c^+. Due to the linear dependence on ϵ, this can be readily calculated taking as a reference the value of γ_c^+ for the longest notch, γ_{sat}—i.e., $\epsilon_{eq}(L_n)=\epsilon\gamma_{sat}/\gamma_c^+(L_n)$. The calculated values for $\epsilon_{eq}(L_n)$ are plotted in Fig. 3 as solid symbols. The result is physically sound, in the sense that the shorter the

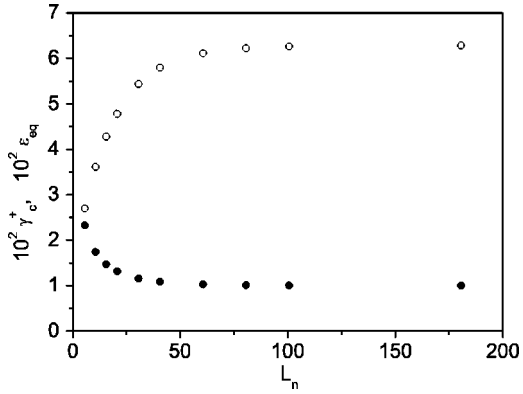

FIG. 3. Notch length dependence of breaking strain threshold (open symbols) and the equivalent externally imposed strain (solid symbols). In the vertical axis, magnitudes are dimensionless, while L_n is in units of lattice spacing.

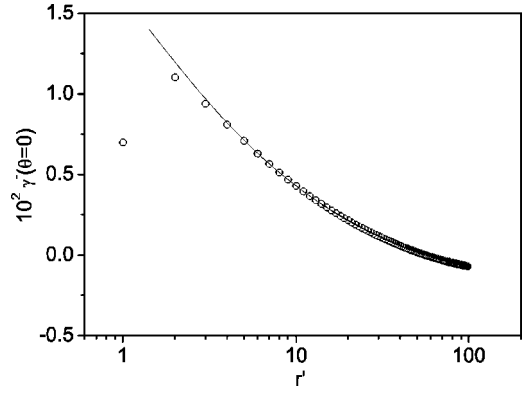

FIG. 4. Linear-logarithmic plot of the radial dependence of γ^- in the direction of straight crack propagation. The line corresponds to the fit to expression (13). Magnitudes are in the selected units.

notch, the higher the strain needed for the crack to start moving. Qualitatively speaking, the saturation of γ_c^+ at long notch length means that the strain field close to the crack tip does not feel anymore the upper free boundary of the plate; i.e., the static strain field at long notches should correspond to the case of an infinite strip. Conversely, for a shorter notch length, the static strain field approaches the configuration corresponding to a semi-infinite strip. This interpretation can be put in a more quantitative way by looking at the strain field close to the crack tip.

Actually, close to the tip (i.e., at distances sufficiently smaller than the strip width), the static stress field should approach the zero-velocity limit of the Yoffe [17] solution for a moving crack in an infinite continuous linear elastic medium under mode-I loading. This null velocity limit coincides with the well-known Irwin-Williams field [5,6]. Accordingly, the static stress field can be represented as

$$\sigma_{ij}(r,\theta) = \frac{K^I}{\sqrt{2\pi r}}\Sigma_{ij}^I(\theta) + \sigma_{ij}^{(1)}, \tag{9}$$

where $\sigma_{ij}^{(1)}$ must be a diagonal tensor to comply with the symmetry requirements of mode-I loading. Both $\sigma_{yy}^{(1)}$, which depends on the crack face traction, and $\sigma_{xx}^{(1)}$ must be computed specifically for each particular deformation problem; moreover, $\sigma_{yy}^{(1)}$ should be higher than $\sigma_{xx}^{(1)}$. The elements of the tensor that reflects the angular dependence of the asymptotic field, $\Sigma_{ij}^I(\theta)$, are

$$\Sigma_{xx}^I(\theta) = \cos\frac{\theta}{2}\left[1 - \sin\frac{\theta}{2}\sin\frac{3\theta}{2}\right],$$

$$\Sigma_{yy}^I(\theta) = \cos\frac{\theta}{2}\left[1 + \sin\frac{\theta}{2}\sin\frac{3\theta}{2}\right],$$

$$\Sigma_{xy}^I(\theta) = \cos\frac{\theta}{2}\sin\frac{\theta}{2}\cos\frac{3\theta}{2}. \tag{10}$$

Then, the strain tensor can be recovered from the classical relationships between strain and stress in the case of plane strain. A full comparison between the spatial structure of the expressions above with the results of the simulations is beyond the scope of this work. Instead, we will just compare the spatial structure of γ^+—that is, the quantity governing the crack motion—with the corresponding results of the simulations. For this purpose it is better to decouple the radial and angular dependences in γ^+. This can be done focusing, on the one hand, on the radial dependence of γ^+ at points such that $\theta=0$ and, on the other hand, on the angular dependence of γ^+ at points located at fixed r. Concerning $\gamma^+(r,\theta=0)$, it is easy to see that $\Sigma_{ij}^I(\theta=0)$ is just the identity matrix, so that

$$\gamma^+(r,\theta=0) = \gamma_{yy} = \frac{1+\nu}{E}\left[(1-2\nu)\frac{K^I}{\sqrt{2\pi r}} + (1-\nu)\sigma_{yy}^{(1)} - \nu\sigma_{xx}^{(1)}\right]. \tag{11}$$

Conversely, for $\gamma^-(r,\theta=0)$, we get

$$\gamma^-(r,\theta=0) = \gamma_{xx} = \frac{1+\nu}{E}\left[(1-2\nu)\frac{K^I}{\sqrt{2\pi r}} + (1-\nu)\sigma_{xx}^{(1)} - \nu\sigma_{yy}^{(1)}\right]. \tag{12}$$

Consequently, for $\theta=0$, both eigenvalues show the same radial dependence: namely, a singular term with the same multiplicative constant, plus an additive constant term, which is different for each eigenvalue. Therefore, fitting the curves of $\gamma^+(r,\theta=0)$ and $\gamma^-(r,\theta=0)$ to such a dependence would allow us to determine K^I, $\sigma_{xx}^{(1)}$, and $\sigma_{yy}^{(1)}$. Such a fitting process must take into account that strain at P_1 is finite and, therefore, the singularity should be considered lagging behind P_1 by a distance r_0.

Linear-logarithmic and logarithmic-logarithmic plots corresponding to $\gamma^-(r,\theta=0)$ and $\gamma^+(r,\theta=0)$ for $L_n=100$ are shown in Figs. 4, 5, 6, and 7, respectively, where the radial coordinate is referred to P_0; i.e., the radial position with respect to P_0 will be $r'=r+1-r_0$. The solid lines represent fits to the expressions

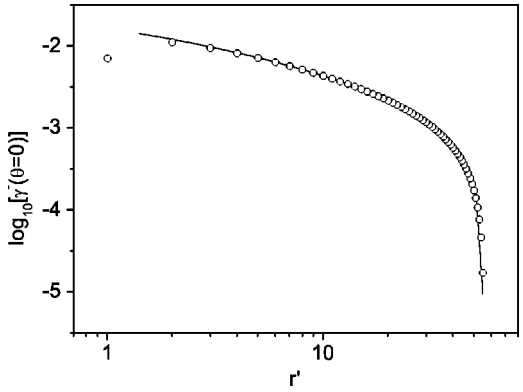

FIG. 5. Double-logarithmic plot of the radial dependence of γ^- in the direction of straight crack propagation. The line corresponds to the fit to expression (13). The values of γ^- have been rescaled by a factor 10^5 for axes labeling purposes. Magnitudes are in the selected units.

$$\gamma^+(r',\theta=0)=\frac{c_1}{\sqrt{2\pi(r'+r_0-1)}}+c_2,$$

$$\gamma^-(r',\theta=0)=\frac{c_1}{\sqrt{2\pi(r'+r_0-1)}}+c_3. \qquad (13)$$

Let us first comment on the behavior of $\gamma^-(r,\theta=0)$. It is apparent from Figs. 4 and 5 that the fit to the expression above is excellent but for the three positions located close to the tip. Hence, one can distinguish two regions with different behavior: at short distances, $\gamma^-(r,\theta=0)$ separates from the expected Irwin-Williams solution, while at intermediate and long distances the fit to the Irwin-Williams solution in Eqs. (13) is rather good, yielding $c_1=0.062$, $r_0=1.63$, and $c_3=-0.0033$. The good quality of the fit at intermediate and long distances is probably due to the fact that the eigenvector corresponding to $\gamma^-(r,\theta=0)$ is parallel to the direction of straight propagation ($\theta=0$) and, in that direction, the effect of the plate boundaries is very small.

In Figs. 6 and 7 we show linear and logarithmic plots of $\gamma^+(r,\theta=0)$. In this case three different regions can be appreciated. First, the region at short distances from the tip ($r'\lesssim 6$) in which the prevalence of the singular term allows for a good fit to just the singular term in Eq. (13) (i.e., with $c_2=0$) to be made. In this region the effects of the lattice topology are important, and the values obtained for constants c_1 and r_0 are different from those obtained from the fit of the $\gamma^-(r,\theta=0)$ curve. Nevertheless, the best fit in this region yields $c_1=0.081$, $r_0=0.27$.

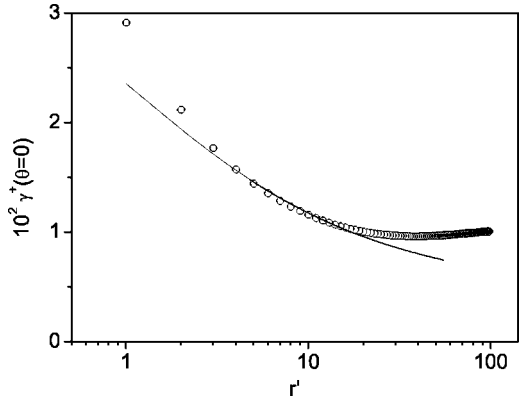

FIG. 6. Linear-logarithmic plot of the radial dependence of γ^+ in the direction of straight crack propagation. The line corresponds to the fit to expression (13) in the intermediate radial range.

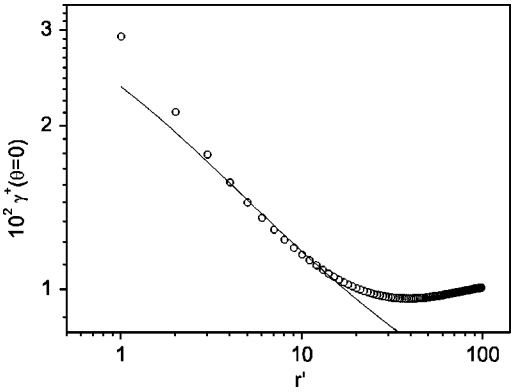

FIG. 7. Double-logarithmic plot of the radial dependence of γ^+ in the direction of straight crack propagation. The line corresponds to the fit to expression (13) in the intermediate radial range.

Second, a long-distance region ($r'\gtrsim 16$) in which nonsingular contributions due to the constant displacement boundary conditions dominate [34]. Third, there is an intermediate region ($6\lesssim r'\lesssim 16$) in which a fit to Eq. (13) gives values of c_1 and r_0 coinciding with those obtained from the fit of the $\gamma^-(r,\theta=0)$ curve, so that $c_1=0.062$, $r_0=1.63$, and $c_2=-0.0041$.

Figures 4, 5, 6, and 7 show that at very short distances from the crack tip the strain values deviate from the trend observed at somewhat deeper points inside the plate. This is not surprising because, close to the tip, the local geometry of the lattice (triangular unit cell; P_1, P_2, and P_3 have only five neighbors) should have important effects. Indeed, one can argue that the lack of bond between lattice site P_0 and sites P_1, P_2, and P_3 is the most relevant aspect of local tip geometry as far as the radial dependence of strain field in the direction of straight propagation is concerned. Actually, Figs. 4 and 5 show that $\gamma^-(r,\theta=0)$—i.e., γ_{xx}—is positive close to the tip and, therefore, the lattice bonds are stretched in the x direction. However, the two bonds that are closer to the crack tip are less stretched in the x direction than the following ones. Obviously, this happens because once the P_0P_1 bond is removed, the node at P_1 is more free to approach the following point ahead of the tip and, then, the strain in the x direction decreases. This decrease penetrates roughly two or three lattice spacings inside the uncracked zone.

A parallel argument can be constructed for $\gamma^+(r,\theta=0)$: once the bonds P_0P_2 and P_0P_3 are removed, part of their corresponding strain in the y direction is transferred to the bonds P_1P_2 and P_1P_3 and, therefore, the strain in the y direction should increase. Again, this increase penetrates roughly two or three lattice spacings inside the uncracked zone (see Figs. 6 and 7). It is conceivable that this strain field behavior (disagreement with linear elasticity results very

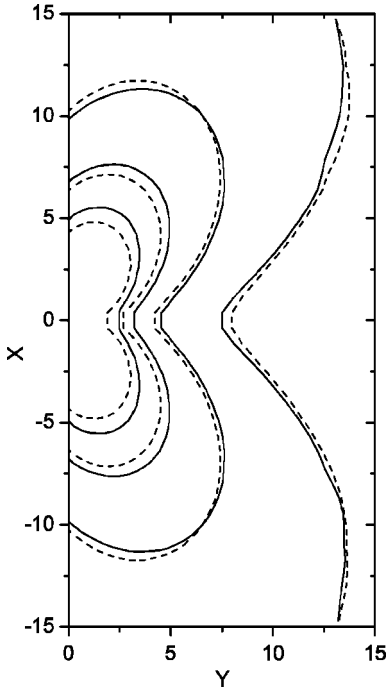

FIG. 8. Two-dimensional contour plot of γ^+ in the intermediate radial range, for a static crack in a plate with $L_n=100$. Solid lines: simulation results. Dashed lines: reconstructed from the Irwin-Williams solution with the values of the parameters taken from the fits of the radial dependences of γ^+ and γ^-. The unit length in both axes is the lattice spacing.

close to the tip) should appear in all fracture lattice models in which the fracture criteria are based on bond cutting procedures that result in diminishing the number of bonds at the crack tip. The penetration depth of this effect might be model dependent, though.

With the values of the constants obtained from the two radial fits corresponding to the intermediate region described above, the full spatial structure of the tensorial strain field can be recovered. In Fig. 8 we show a contour plot of the two-dimensional structure of $\gamma^+(r,\theta)$, in which solid and dashed lines correspond, respectively, to the numerical results and the Irwin-Williams solution with parameters r_0, c_1, and c_2 as obtained from the previous fits for the intermediate range of the radial coordinate. In this plot, each pair of solid and dashed lines corresponds to the same contour level. The differences between consecutive contour levels are about 10% of the level value; therefore, the differences at each level between the numerical and analytical values are smaller than 5%. Hence, the agreement between the spatial structure obtained in the simulation results and the Irwin-Williams solution is remarkable. An aspect of the static strain field which is of primary importance for the crack dynamics is the influence of L_n on the radial structure of $\gamma^+(\theta=0)$. In Fig. 9 we plot $\gamma^+(r,\theta=0)$, at different values of L_n. The most salient feature of this figure is that the strain field gets flatter the shorter the notch. Actually, decreasing the notch length makes the structure of the singularity less visible.

Casting these curves (see Fig. 10) in terms of plates breaking at the same value of γ^+, as was done above for the analysis of Fig. 3, would result in all curves having the same value at the lowest r and shifting upwards the rest of the curves; this shift will be higher the shorter the notch.

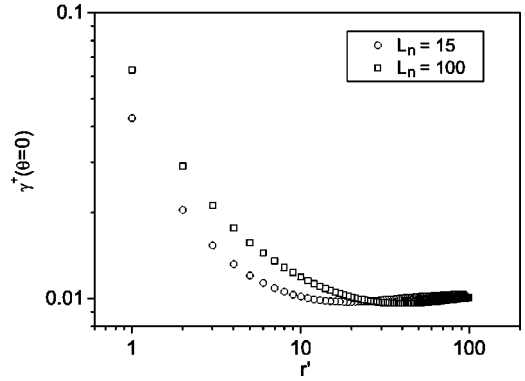

FIG. 9. Comparison of the radial dependences of $\gamma^+(\theta=0,v=0)$ for plates with two different initial notch lengths.

For large values of L_n, the curves superpose rather well, which suggests that for long notches the strain field structure ahead of the crack tip does not feel the existence of the upper free boundary of the plate, so that the situation corresponds effectively to a crack in an infinite strip.

IV. DYNAMICS

A. Fracture patterns

In Figs. 11 and 12 we show the spatial patterns obtained at increasing values of L_n. Some common features can be recognized in them: the cracks propagate in a straight line, until branching occurs. The length of straight propagation part is larger for increasing values of L_n as shown in Fig. 13; we will show below that this fact is connected with the acceleration of the crack, which is smaller the longer L_n. The constant value of the straight crack length at large notch length confirms the close correspondence of that situation to the case of an infinite strip.

The complexity of the crack pattern increases as L_n decreases, showing more branches which survive longer and

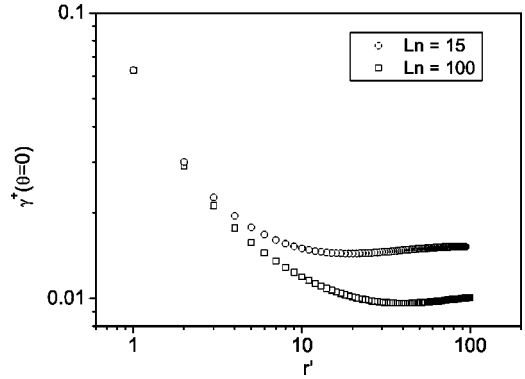

FIG. 10. Comparison of the radial dependences of $\gamma^+(\theta=0,v=0)$ for plates with two different initial notch lengths. Curves have been rescaled in the ordinate axis to mimic plates breaking at the same breaking strain threshold.

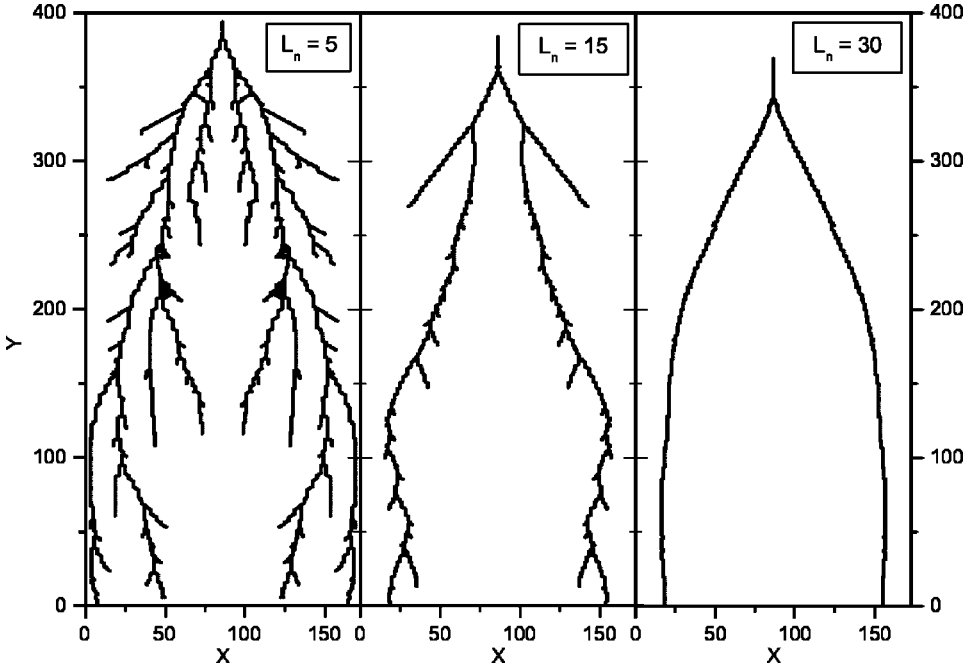

FIG. 11. Fracture patterns obtained in plates with short initial notches. The simulation is stopped when a symmetric pair of cracks arrives at the bottom end of the plate. The unit length in both axes is the lattice spacing.

that show further branching events. This increased branching at low values of L_n can be qualitatively understood in terms of the strain (or stress) field. For shorter notches, the relevance of the notch is smaller and the strain field becomes increasingly flat [33]; i.e., the plate is more evenly strained in the sense that the differences in strain across the plate are smaller and, therefore, all of the nodes are closer to the disconnection threshold than in a long-notched plate. When the crack motion starts, waves propagate into the plate and along the crack lips. It has been argued [13] that such waves, after reflection at the plate boundaries, might trigger branching at the crack tip. In the simulations reported here such a mechanism might appear as follows: the reflected waves cause perturbations of the strain field that may help to overcome the breaking threshold at positions out of the local direction of straight propagation, giving rise to branching. This mechanism may be particularly relevant in the case of moderately flat strain fields, such as those appearing at low values of L_n.

We have checked the time of arrival of bulk waves and Rayleigh waves to the advancing crack tip in all of the simulations here considered. The labels in Table I refer to the time at which the first branching event occurs in the simulations, t_{b1}^{sim}, the time of arrival to the position at which branching occurs of a longitudinal (respectively transversal) wave generated in the first disconnection event reflected at the upper boundary, $t_{\parallel}^{u}$ (respectively, $t_{\perp}^{u}$), the time of arrival to the position at which branching occurs of a Rayleigh wave generated in the first disconnection event reflected back at the

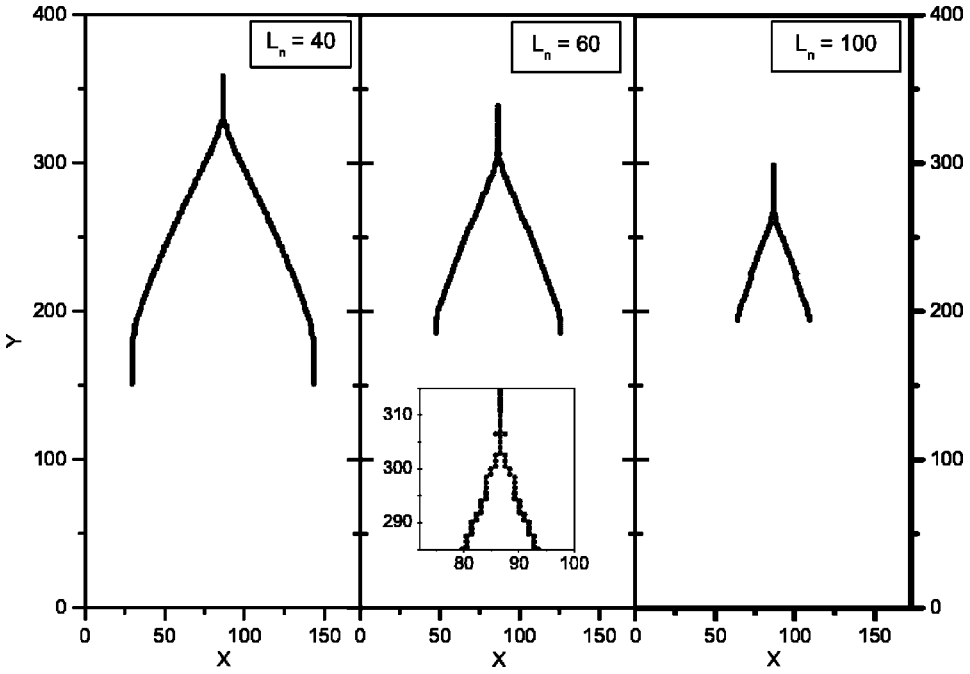

FIG. 12. Fracture patterns obtained in plates with long initial notches. Simulations are stopped long time after crack arrest occurs. The inset shows attempted branching. The unit length in both axis is the lattice spacing.

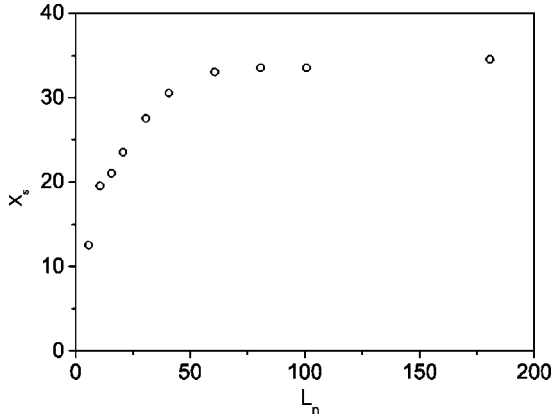

FIG. 13. Length of the straight propagation part of the crack as a function of notch length L_n. The unit length in both axis is the lattice spacing.

upper boundary, t_R^u, and the time of arrival to the position at which branching occurs of a longitudinal (respectively, transversal) wave generated in the first disconnection event reflected at any of the lateral boundaries, $t_{\|}^l$ (respectively, $t_{\perp}^l$). The results quoted in Table I show that, in all of the cases, the first branching event is not coincident with the arrival of any of the waves considered—namely, longitudinal and transversal waves reflected at either the upper or lateral surfaces of the plate and Rayleigh waves reflected at the upper surface.

Interestingly enough, the second branching event occurring in the cases of low values of L_n coincides, within the simulation error, with the arrival of the Rayleigh wave generated at the first disconnection event to the crack tip after reflection at the upper surface of the plate. This is shown in Table II, where t_{b2}^{sim} refers to the time at which the second branching event occurs in the simulations and t_R^u refers now to the time of arrival to the position at which the second branching event occurs of a Rayleigh wave generated in the first disconnection event reflected back at the upper boundary.

TABLE I. Time of arrival of bulk and surface waves at the point where the first branching occurs as a function of L_n. t_{b1}^{sim} refers to the time obtained in the corresponding simulation. Subscripts $\|$, $\perp$, and R refer to longitudinal, transversal, and Rayleigh waves, respectively. Superscripts u and l refer to waves reflected in the upper and lateral plate boundaries, respectively.

L_n	t_{b1}^{sim}	$t_{\|}^u$	$t_{\perp}^u$	t_R^u	$t_{\|}^l$	$t_{\perp}^l$
5	19.622	12.4	21.5	23.5	91.7	158.8
10	29.278	21.34	37.0	40.5	92.0	159.4
15	35.834	27.5	47.6	52.0	92.1	159.6
20	41.964	34.1	59.0	64.5	92.3	159.8
30	50.508	46.7	80.9	88.5	92.6	160.4
40	56.628	58.9	102.0	111.5	92.8	160.8
60	61.198	81.3	140.8	154.0	93.1	161.2
80	63.232	102.7	177.9	194.0	93.1	161.3
100	63.454	123.8	214.4	234.5	93.1	161.3
160	65.0	208.8	361.7	395.5	93.2	161.5

TABLE II. Time of arrival of surface waves at the point where the second branching occurs as a function of L_n. t_{b2}^{sim} refers to the time obtained in the corresponding simulation. t_R^u refers to the Rayleigh wave traveling along the crack lip and reflected in the upper plate boundary.

L_n	t_{b2}^{sim}	t_R^u
5	47.50	46.56
10	72.07	72.64
15	93.55	95.13
20	112.73	115.54
30	181.05	180.50

At large values of L_n, only one branching event occurs. The two branches separate initially, but after some time they get oriented parallel to the initial notch. In all of these cases, crack arrest occurs simultaneously for both parallel running cracks. Obviously, the energy flow towards the crack tips is not enough to support the motion of two parallel running cracks. Note that symmetry with respect to the notch line is fully preserved during the whole crack propagation process even in the most complex patterns here obtained, showing the quality of the simulations carried out with the fracture criterion here proposed. In a more general case of nonfully symmetric initial conditions or when disorder is included, one would expect that one of the cracks would be more advanced than the other one and that only the most advanced crack would survive.

Two other aspects of the fracture patterns are worth mentioning. First, attempted branching may appear, in the sense that in some runs points P_1, P_2, and P_3 may become disconnected at the same time step. This means that all of the three points go above the disconnection threshold simultaneously for that time step. In such cases (see, for instance, the patterns for $L_n=15$ and $L_n=60$ in Fig. 11 and the inset in Fig. 12, respectively) the subsequent evolution does not show branching but straight propagation again until a regular (macroscopic) branching event occurs. The simultaneous disconnection at the three tip points always disappears when the time step is decreased. Therefore attempted branching is caused merely by insufficient resolution in the time step. Nevertheless, the appearance of attempted branching shows that, in some dynamical conditions, the values of γ^+ at points P_1, P_2, and P_3 are very close to each other so that, again, a small amount of disorder may trigger the appearance of attempted branching just before macroscopic branching occurs.

Second, at the shortest notch, the combined effect of the high strain all through the plate and wave emission causes that the fracture process can continue even after the two symmetrically running cracks have arrived to the bottom of the plate. This can be seen in Fig. 14, where the simulation has been continued after the plate is fully broken. Figure 11 shows the corresponding fracture pattern at the time that the two most advanced symmetrically running cracks arrive to the bottom of the plate. The comparison of these two figures clearly shows that disconnection events still occur much after the plate is divided in three separate parts, giving rise

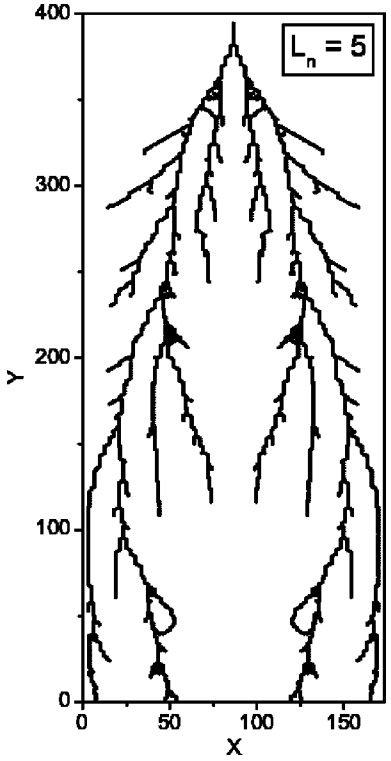

FIG. 14. Fracture patterns obtained in plates with a very short initial notch ($L_n=5$). This is a continuation of the simulation corresponding to the first pattern in Fig. 11 until no more disconnection events occur.

even to closed loops that produce some debris.

B. Kinematics of straight crack motion

1. Velocity

In order to study the velocity of the crack tip, when the crack is in straight motion, we define the position of the tip as the position of the breaking node at a given time. The tip velocity is then calculated by dividing the y coordinate difference by the time interval separating the last two events of node disconnection. The time history of the velocity for the crack tip during straight propagation, for different values of L_n is shown in Fig. 15.

In all of the cases, the first value obtained for the crack velocity is larger than 0.37 (in units of v_R). This is in agreement with observations in other simulations [15,27,35] and might suggest the existence of a minimal crack velocity, although experimental results in PMMA [36] and single-crystal silicon [37] seem not to support this effect. In Fig. 16 we present the crack speed evolution corresponding to the case $L_n=100$ in Fig. 11, together with the same evolution obtained in a similar plate of spatial resolution twice higher ($L_x=200\sqrt{3}$, $L_y=800$, $L_n=200$) than in the previous pictures. Note that, in this figure, the time axis has been rescaled for the high-resolution plate (the time unit here is a/V_R; therefore, doubling the number of lattice sites means halving a and also halving the time unit).

Remarkably, both curves superpose rather well: the initial velocity is slightly above 0.37; then, the velocity increases slowly to a tip speed of about 0.4, at which a sudden increase up to a velocity value above 0.55 occurs.

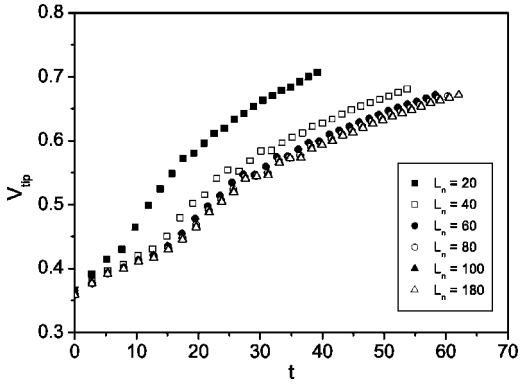

FIG. 15. Crack tip velocity as a function of time for different notch lengths. After the last time recorded, branching takes place. Units are the lattice spacing a and the Rayleigh velocity v_R.

2. Acceleration

As the tip motion proceeds, its velocity shows some ripples superimposed onto an increasing trend. The crack tip acceleration then shows fluctuations around a roughly constant value. In Fig. 17, we plot the acceleration $\ddot{x}(t)$ of the crack tip against time for the low-resolution, long-notch plate ($L_x=100\sqrt{3}$, $L_y=400$, $L_n=100$). Generally speaking, the values of the tip acceleration are larger the shorter the initial notch.

The fine details can be better appreciated in Fig. 18, where we plot the acceleration corresponding to the high-resolution equivalent plate ($L_x=200\sqrt{3}$, $L_y=800$, $L_n=200$). In this case both the time and acceleration axes have been rescaled to allow for proper comparison. The initial evolution of the acceleration in both the high- and low-resolution plates is quite similar. However, at $t\geqslant 20$ in rescaled time units, the acceleration shows strong fluctuations, going even negative.

The origin of the oscillations in the tip acceleration is not completely clear, but an interpretation in terms of wave emission at the crack tip is appealing [38]. When looking at

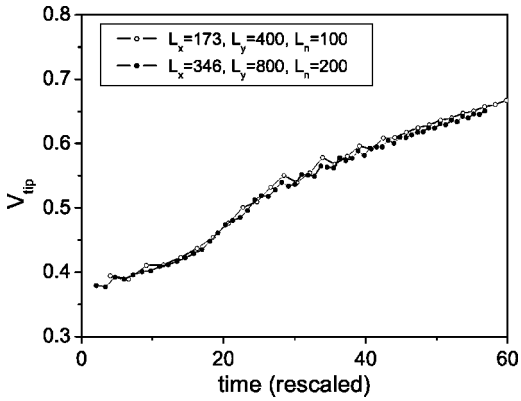

FIG. 16. Comparison of the temporal evolution of the crack tip velocity between similar plates with different spatial resolution. The temporal coordinate for the high-resolution plate has been rescaled according to the time unit chosen (a/V_R).

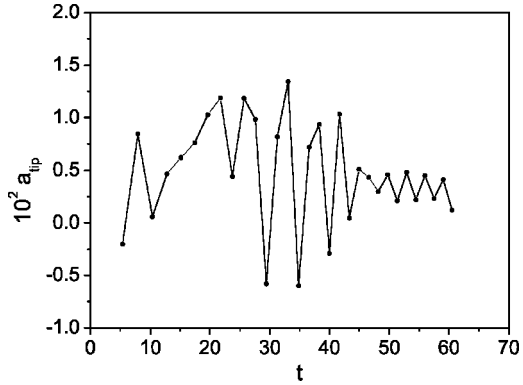

FIG. 17. Acceleration of the crack tip for a plate with $L_x=100\sqrt{3}$, $L_y=400$, $L_n=100$.

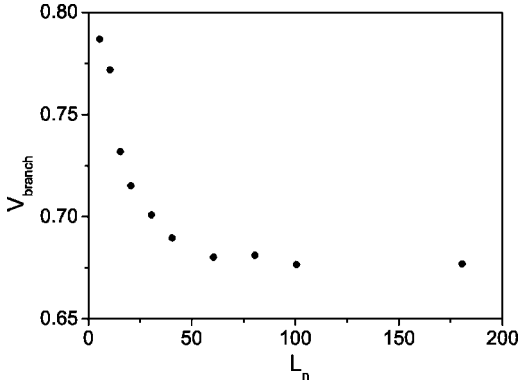

FIG. 19. Velocity threshold for branching as a function of notch length.

the acceleration curve for the high-resolution plate, one may distinguish two time regions in which the acceleration goes negative: namely the intervals $30 \leqslant t \leqslant 40$ and $50 \leqslant t \leqslant 60$. Inside both time intervals the ripples in the acceleration are much more periodic, the period at each interval being, approximately, 2.65 ± 0.05 and 1.56 ± 0.02 rescaled time units, respectively. In these time intervals the values of the tip velocity are 0.56 ± 0.01 and 0.64 ± 0.01, respectively. The combination of these time intervals and tip velocities would give effective wavelengths of 1.48 ± 0.08 ($\simeq 3/2$) and 1.0 ± 0.03, respectively. This fact points to a mechanism involving radiation of waves with wavelengths that are semi-integer multiples of the lattice spacing, in qualitative agreement with the results reported in Ref. [15]. A comparison with the results reported in Ref. [16] is not possible though, due to the inherent difference of both problems. In Ref. [16], the crack velocity is set in each run by cutting bonds at a prescribed rate and the waves are studied by means of the displacement field at the lip of the crack. Instead, in this work the crack velocity is governed by the strain field dynamics and the waves emitted at the disconnection events also affect the crack tip velocity.

C. Branching instability

1. Velocity threshold

Branching occurs when a straight propagating crack reaches a given speed. In Fig. 19 we plot the speed at which branching occurs as a function of notch length. For long notches ($L_n \gtrsim 40$)—i.e., when the problems is analogous to a crack in an infinite strip—there is a well-defined threshold value of the branching speed $V_c=0.675 \pm 0.002$.

This behavior is analogous to the one reported in [25], for the same problem with a nonsymmetrical notch, although the value obtained for the branching speed was then $V_c=0.71 \pm 0.01$. In the present study we have extended the analysis to much shorter notches. There a strong dependence of the branching velocity on notch length appears, reflecting the different character of the problem, which approaches the semi-infinite strip problem as the notch gets shorter.

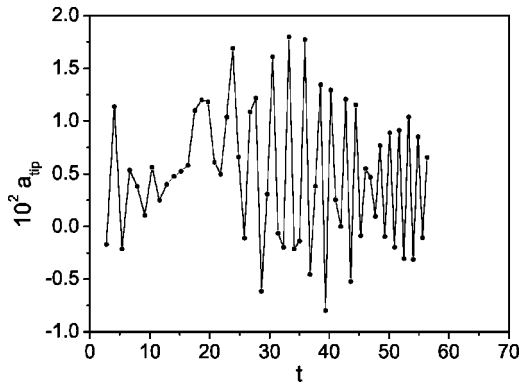

FIG. 18. Acceleration of the crack tip for a plate with $L_x=200\sqrt{3}$, $L_y=800$, $L_n=200$.

2. Branch angle

Due to the triangular lattice structure, the first nodes to be disconnected when the crack branches are always at 60° from the straight propagation direction. The subsequent crack evolution does not follow a lattice direction but, as can be seen in Fig. 12, a straight line with a well-defined average angle. We have calculated the average angle α formed by each branch with respect to the direction of straight propagation in the initial part of the branch. First, we remark that in all of the simulations, α does not correspond to a lattice direction. The values obtained show some scatter, as shown in Fig. 20, although all of them lie in the range between 18° and 24°, which compare fairly well with experimental values [8]. Interestingly, recent theoretical work on the branching instability under general loading predicts a branching angle of 23.4° for an elastic solid with Poisson ratio of 0.25 by assuming that the principle of local symmetry holds [19]. Similar values for the branching angle have been obtained in a phase field model for elastic fracture [39], in which the principle of local symmetry is respected.

Yoffe's asymptotic solution for the stress field around an advancing crack has been extensively used to discuss the branching instability. However, its direct applicability to interprete a branching instability in a discrete model seems to be dubious. Basically, two different branching criteria stem from Yoffe's solution. The criterion based on the maximal hoop stress predicts branching at a critical velocity. At this critical velocity, the branching angle is 0° [25]. Above the critical velocity, the branching angle increases continuously

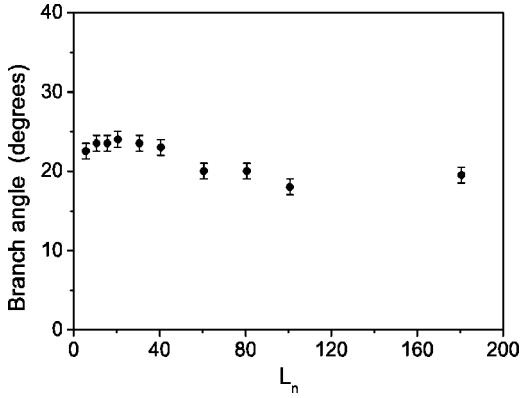

FIG. 20. Branch angle as a function of notch length.

with the crack tip velocity. On the other hand, the criterion based on the maximum eigenvalue of the stress field predicts a branching angle close to 60° for any nonzero crack tip velocity [5]. According to this criterion, a dynamic crack would always branch at approximately 60° from the very moment it starts moving. None of these criteria can account for the observed values of the average branching angle.

V. QUALITATIVE EXPLANATION FOR THE BRANCHING INSTABILITY

In this section we propose a qualitative explanation of the branching instability in discrete lattices. We remark that this is only a kinematic model; a dynamic theory should account for the acceleration due to the energy balance close to the tip. In this sense, the disconnection of the particles is merely a particular energy dissipation mechanism at the tip, which should play a role regarding the acceleration of the crack, but not on the branching mechanism.

A. General model: Branching of a moving crack in a discrete Yoffe's stress field

The question, is while the singularity tip moves forward at constant speed v, can $\gamma^+(\mathbf{r},v)$ go above threshold at point P_2 before it does at point P_1 (see Fig. 2)? To answer this question we will analyze a model problem: the evolution of the Yoffe's stress field of a crack moving at constant speed in a triangular lattice. More explicitly, let us consider a crack whose singularity moves at given speed v in a discrete medium with the lattice structure shown in Fig. 2. Let us label with suffix 1 the quantities referring to the particle in the geometrical tip apex, with suffix 2 the two symmetrical adjacent particles, and with suffix 0 the particle placed in the straight propagation direction before particle 1 (see Fig. 2). The position of the singularity with respect to particle 0 is $r_0(v)$. Let us also assume that Yoffe's stress field is a reasonable representation for the stress field at the positions occupied by the particles [17]. In all of the following the tensorial magnitudes are always the highest eigenvalues of the corresponding tensors; therefore, we drop the + superscript, and distances and time are made dimensionless as in the previous sections of this paper.

First of all, one has to realize that, for Yoffe's stress field, the threshold condition for the highest eigenvalue of the stress tensor reads

$$\sigma^Y(r,\theta,v,t) = \frac{K^I(t)}{\sqrt{2\pi r_0[v(t)]}}\Sigma^I(\theta,v) = \sigma_c.$$

The threshold value σ_c is set as the value of σ^+ at the geometrical tip at $t=0$ (and, therefore, $v=0$); then,

$$\sigma_c = \frac{K^I(t)}{\sqrt{2\pi r_0(0)}}\Sigma^I(\theta=0,v=0) = \frac{K^I(0)\Sigma^Y(0,0)}{\sqrt{2\pi r_0(0)}}. \quad (14)$$

The influence of the notch length should appear in the expression above as a dependence of $r_0(0)$ on notch length and, eventually, as slight deviations of $\Sigma^{sim}(\theta,v=0)$ from $\Sigma^Y(\theta,v=0)$.

Then, in the time interval of interest, $r_1(t)=r_0(v)+1-vt$, and $\theta_1=0$, so that

$$\sigma_1(t) = \sigma^Y(r_1(t),\theta_1,v) = \frac{K^I(t)}{\sqrt{2\pi r_1(t)}}\Sigma^Y(\theta_1,v)$$

$$= \frac{K^I(t)}{\sqrt{2\pi[r_0(v)+1-vt]}}\Sigma^Y(0,v). \quad (15)$$

Using the threshold condition for particle 1 we get

$$\frac{K^I(t)\Sigma^Y(0,v)}{K^I(0)\Sigma^Y(0,0)} = \sqrt{\frac{r_0(v)+1-vt}{r_0(0)}}. \quad (16)$$

Therefore, the time at which the point P_1 would be disconnected—namely, t_1—can be obtained as

$$t_1 = \frac{1}{v}\left[1 + r_0(v) - r_0(0)\left(\frac{K^I(t)\Sigma^Y(0,v)}{K^I(0)\Sigma^Y(0,0)}\right)^2\right]. \quad (17)$$

Generally speaking, the dependence of $r_0(v)$ on velocity in a discrete medium would be related to the stress (or strain) field dynamics. In the model problem considered in this section, the $r_0(v)$ dependence on velocity is fully determined by the evolution of Yoffe's stress field. In such a case, at time t_1, the distance of P_1 to the singularity must be $r_0(v)$, so that the application of the threshold condition yields

$$r_0(v) = r_0(0)\left(\frac{K^I(t)\Sigma^Y(0,v)}{K^I(0)\Sigma^Y(0,0)}\right)^2. \quad (18)$$

Straightforward algebra then leads to the trivial solution $t_1=1/v$. On the other hand, the position of point P_2 referred to P_0 is described by (see Fig. 2)

$$r_2(t) = \sqrt{(\sin\theta_l)^2 + [r_0(v)+1-vt]^2}, \quad (19)$$

where $\theta_l=\pi/3$ for a triangular lattice and

$$\theta_2(t) = \arctan\frac{\sin\theta_l}{r_0(v)+\cos\theta_l - vt}, \quad (20)$$

so that [40]

$$\sigma_2(t) = \sigma^Y(r_2(t),\theta_2(t),v) = \frac{K^I(t)\Sigma^Y(\theta_2(t),v)}{\sqrt{2\pi r_2(t)}} \quad (21)$$

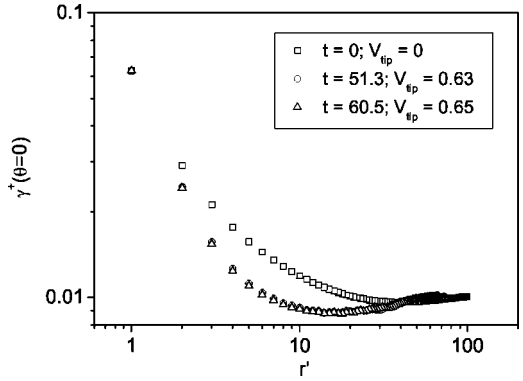

FIG. 21. Snapshots of the radial dependence of $\gamma^+(\theta=0,v)$, in the case $L_n=100$, at the times in which the tip velocity is, respectively, $v=0$ (squares), $v=0.60$ (circles), and $v=0.65$ (triangles).

$$= \frac{K^I(t)\Sigma^Y\left(\arctan\dfrac{\sin\theta_l}{r_0(v)+\cos\theta_l - vt}, v\right)}{\sqrt{2\pi\sqrt{(\sin\theta_l)^2+[r_0(v)+\cos\theta_l - vt]^2}}}. \quad (22)$$

Using the threshold condition for particle 2 we get

$$\frac{K^I(t)\Sigma^Y(\theta_2(t),v)}{K^I(0)\Sigma^Y(0,0)} = \sqrt{\frac{r_2(t)}{r_0(0)}}. \quad (23)$$

Equation (23) can be solved numerically in order to obtain t_2. Therefore, if $t_1<t_2$, straight propagation occurs; on the other hand, if $t_1>t_2$, branching occurs, so this model allows qualitatively for branching.

B. Numerical estimations

The model described above is formulated in terms of the stress field; however, with the help of the plane strain relationships it can be easily formulated in terms of the strain field. The predictions of the model depend critically on the values of $r_0(0)$ and $r_0(v)$. In Fig. 21 we show the appearance of the radial dependence of $\gamma^+(r,\theta=0,v)$, in the case $L_n=100$, for three different values of v: namely, $v=0$, $v=0.60$, and $v=0.65$. Note that for the moving cracks, the nonsingular terms are due to the strain field dynamics [41] and not to the constant-displacement boundary conditions.

These results show that, at high crack tip speed, the $\gamma^+(r,\theta=0,v)$ curve does not change significantly upon an increase of the tip velocity, because the curves for $v=0.60$ and $v=0.65$ coincide with each other up to quite a long distance from the tip. Therefore, we can make some estimations by taking the values of $r_0(0)$ and $r_0(v)$ from fits of the curves shown in Fig. 21, in the region close to the crack tip, to the form

$$\gamma^+(r',\theta=0,v) = \frac{c_1}{\sqrt{2\pi(r'+r_0(v)-1)}}. \quad (24)$$

The results of these fits are summarized in Table III.

In Fig. 22 we plot the dependence of t_1 (dotted line) and t_2 (dashed line) on the tip velocity using the values given in Table III for $v=0.65$. For values of the tip speed so that $V_{tip}<0.675$, only the point at the tip—i.e., P_1—goes above the disconnection threshold, because the equation determining t_2 does not have a real solution. Therefore branching can not happen and straight propagation is predicted. In the interval $0.675\leqslant V_{tip}\leqslant 0.678$, the point P_2 can go above threshold, but $t_1<t_2$, so that straight propagation is predicted too, although the difference between the values of γ^+ at points P_1 and P_2 is very small and, consequently, small amounts of disorder might trigger branching. At $V_{tip}=0.680$, t_2 becomes smaller than t_1 and, therefore, branching is predicted. This critical value of the tip velocity for branching compares very well with the one obtained in our simulations ($V_{crit}=0.675$).

TABLE III. Results of fitting the curves in Fig. (21) to Eq. (24).

v	c_1	r_0
0.0	0.081	0.27
0.60	0.061	0.15
0.65	0.060	0.14

For the purposes of illustrating the behavior of this model we also show in Fig. 22 the effect of small changes in $r_0(v)$. The solid line in Fig. 22 corresponds to a value of $r_0(v)=0.175$ while the dot-dashed line corresponds to $r_0(v)=0.21$. By increasing $r_0(v)$ the critical branching velocity decreases and the region in which branching is expected widens.

The interplay between t_1 and t_2 is better understood by looking at Fig. 23, where we show the evolution of γ_1^+ and γ_2^+ with time as the tip moves forward at the prescribed velocity. The curves in Fig. 23 correspond to the case $r_0(v)=0.175$ for which the critical branching velocity is $V_{crit}=0.62$. For $V_{tip}\leqslant V_{crit}$, the curve corresponding to $\gamma_2^+(t)$ has a maximum which lies below the value of the disconnection threshold γ_c^+. Therefore, branching can never occur for this range of tip velocities. On the other hand, if the tip velocity is above the critical value for branching, the maximum of the curve corresponding to $\gamma_2^+(t)$ is already above the threshold value for disconnection. Moreover, the curve $\gamma_2^+(t)$ crosses the value γ_c^+ before $\gamma_1^+(t)$ does, so that branching occurs.

For the sake of completeness, we have also looked at the effect of the Poisson coefficient. In Fig. 24 we show the

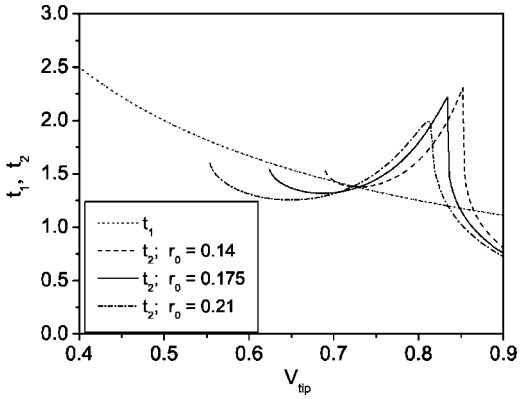

FIG. 22. Dependence of the disconnection times t_1 and t_2 on tip velocity for different values of $r_0(v)$. Magnitudes in selected units.

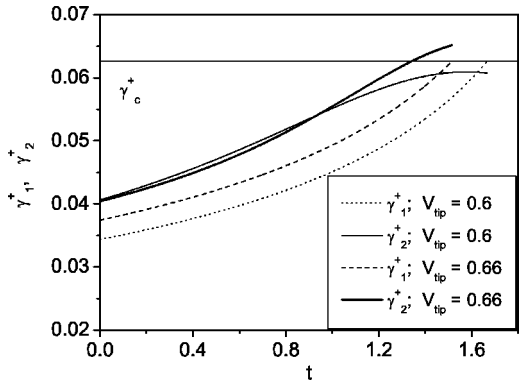

FIG. 23. Comparison of curves $\gamma_1^+(t)$ and $\gamma_2^+(t)$ for values of the tip velocity slightly below and above the branching velocity threshold for the case $r_0(v)=0.175$.

results obtained when setting the value $\nu=0.33$, much closer to the experiments in glass or PMMA, and $r_0(v)=0.175$. Evidently, increasing the value of the Poisson coefficient dramatically lowers the values of the velocity branching threshold.

VI. DISCUSSION

First of all, let us emphasize again that the present implementation of both the fracture criterion and lattice topology allows for a full conservation of the mirror symmetry with respect to the middle vertical plane. Therefore, all of the simulations reported here are strictly under mode-I loading.

Effects of the lattice topology close to the crack tip are apparent, however, as shown also in Ref. [25]. These effects appear as deviations of the radial dependence of the strain field close to the tip from the intermediate distance behavior. In this sense, the radial dependence of the highest eigenvalue of the strain tensor at $\theta=0$ is not of great help as a check for the predictions of linear elastic fracture mechanics (LEFM), because it shows strong nonsingular contributions due to the particular loading configuration, which consists in applying constant displacement at the lateral plate boundaries. Conversely, the lowest eigenvalue yields a very nice agreement

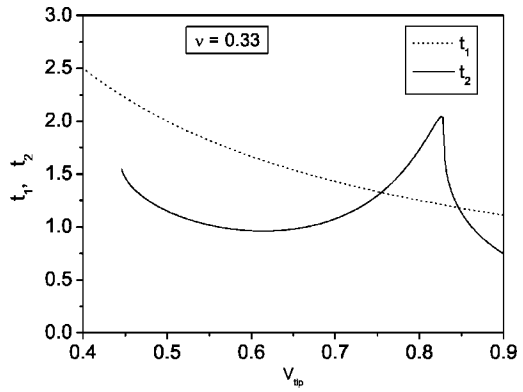

FIG. 24. Illustration of the tip velocity dependence of disconnection times t_1 and t_2 for a plate of a material with $\nu=0.33$ and with the same radial dependence of γ^+ $[r_0(v)=0.175]$.

with the predictions of LEFM, at least in static conditions and slightly away (three to four lattice spacings) from the crack tip. The possibility of reconstructing the full two-dimensional structure of the strain field, although in a restricted distance range, just by taking three parameters from the radial dependence fits shows that the angular structure of the strain field is very well represented by the Irwin-Williams solution. Extending the range of the comparison is not possible because the Irwin-Williams solution pertains to the situation in which the loading configuration corresponds to constant stress at the boundaries of an infinite plate.

Several aspects of the dynamics deserve some comments. For instance, the effect of notch length in the dynamics of the crack can be summarized as follows. Short notches give rise to a structure of the strain field with comparatively smaller strain differences across the plate. This results in dynamical behavior, with high crack tip acceleration, which strongly depends on notch length and which is strongly sensitive to disorder and/or wave propagation. Conversely, long notches $(L_n \gtrsim L_x/2)$ show a behavior independent of notch length because they are close to the model problem situation of a crack in an infinite strip. In this case, the strain differences across the plate are large and, therefore, they are weakly sensitive to perturbations such as disorder and/or wave propagation, unless the crack tip kinematics makes γ_2^+ to become close to γ_c^+.

The speed of the cracks, when in straight motion, is larger than usually found in experiments with glass or PMMA. In the Griffiths picture of fracture, the crack velocity depends on the relationship between energy flow to the tip and energy dissipation at the tip due to crack lip surface creation. Energy flow to the tip is generally ruled by the dynamics of the strain field while, in this model, the energy dissipation at the tip is implicitly determined when the fracture criterion is specified, because the fracture criterion sets the crack lip length created in each disconnection event. Therefore, in this model, the energy dissipation at the tip is not easy to change in a controlled way unless friction is included. However, it is clear from these simulations that crack lip surface creation is not the only mechanism that plays a role in the selection of the crack velocity. Indeed, surface waves have been shown here to have a main role in the time history of the tip velocity and, most importantly, in the appearance of the second branching instability.

It must be kept in mind that the nearest-neighbor discretization scheme reported here is unstable for values of the Poisson ratio strictly higher than $1/4$. Therefore, a full comparison of velocity values with experiments in glass or PMMA, for which $\nu \simeq 0.33$, cannot be made. However, the same optimization scheme used here to derive the equations ruling the dynamics of the lattice sites can be carried out under the assumption of a next-nearest-neighbor interaction. Preliminary numerical results show that this approach eliminates the scheme's stability problem above $\nu=1/4$. Exploiting that scheme would be the object of future work.

In this discrete model, two radically different branching instabilities may appear: one driven by the changes in the strain field caused by the kinematics of the effective singularity and another one triggered by the surface waves produced in the disconnection events, which travel through the

crack lip and are reflected back towards the crack tip. In the plates simulated here, the crack velocities are not small ($V_{tip} \geqslant 0.4V_R$) and the kinematic instability occurs before the surface wave induced instability can take place. This scenario may change easily, for instance, in the case the straight propagation velocities were smaller. In such a case, kinematic branching might be forbidden and the backscattered surface wave would have the time to catch up with the crack tip again. This would be a much closer scenario to experiments [13]. Moreover, in this later scenario, disorder or reflected waves can trigger attempted branching before the surface wave induced branching occurs provided that γ_2^+ is below but close to γ_c^+.

However, it is an experimental fact that in PMMA cracks with very long initial notches may travel through the plate at low constant velocity, without branching. In such cases, kinematic branching should be forbidden and back-reflected surface waves should certainly catch up with the crack tip without producing branching. This type of behavior has not appeared in our simulations. Several mechanisms may be conjectured as ways of solving this model flaw. One is, as stated before, including some dissipation in the model; another one is correcting the "excessive brittleness" of the model (too much energy is released suddenly when a node is disconnected) by means of including some cohesive zone at the crack tip.

Another issue to be considered here is the effect of the spatial resolution in the simulations. The simulations show that increasing the spatial resolution does not affect the dynamics, with the only change of allowing for a more precise study of the effect of surface waves on the crack tip kinematics. This might be surprising because one might naively think that improving the spatial resolution close to the singularity would result in larger strain differences across the plate as points closer to the singularity should "feel" clearly the $1/\sqrt{r}$ divergence. This in turn should modify the abovementioned distinction between short-notch and long-notch consequences as far as sensitivity to disorder and/or wave motion is concerned. This is not so because being correct that strain differences across the plate increase with the spatial resolution, it is also true that the energy released in each disconnection event correspondingly increases with the spatial resolution, yielding an unchanged dynamical scenario.

In our simulations, we have a fracture criteria on the maximum eigenvalue $\Sigma^+(\theta,v)$ of the strain field. It is important to realize that the angular structure of $\Sigma^+(\theta,v)$ of the Yoffe solution by itself cannot explain the branching instability observed in the simulations. In a continuum description represented by the Yoffe solution the structure of $\Sigma^+(\theta,v)$ presents a lateral maximum of higher amplitude than $\Sigma^+(0,v)$ at all velocities but very high ones (see Fig. 4.3 of Ref. [5]). Then, a fracture criterion on $\Sigma^+(\theta,v)$ would imply that branching occurs even at zero crack tip velocity because of the presence of maxima at $\approx 60^\circ$ in $\Sigma^+(0,v=0)$. We have shown that the actual node values of the stress and strain fields do not differ much from those given by Yoffe. Nevertheless, branching is observed only beyond a certain critical velocity. We have explained this fact by assuming that the singularity of the stress field moves at the crack tip velocity and looking at the actual values of the strain field at the discrete node locations. The key point in this kinematic explanation is the analysis of the disconnection times of the nodes ahead and aside of the crack tip. Above certain critical crack tip velocity, the nodes aside of the crack direction have a shorter disconnection time than the node ahead, and branching occurs. It is the combined action of the angular structure of $\Sigma^+(\theta,v)$, the radial dependence of the stress field singularity, and the lattice discreteness which leads to branching for tip velocities above a critical one.

One comment about the model for the kinematic branching instability is in order here. We remark that all of the expressions used in the formulation of the model are made dimensionless with a characteristic length scale that is precisely the lattice spacing. Therefore, these expressions are valid at any spatial resolution, and that means that the critical tip speed values obtained with this analysis are valid for no matter how small the spatial resolution would be.

Understanding, even qualitatively, the values of the branching angle and the competition between parallel running cracks, appearing in the cases of plates with long notches, is still work to be done. At present we do not have an understanding of the values obtained for the branching angle. However, we point out that for long initial notches the values obtained coincide with the experimental ones within the error bars [8]. This fact suggests that, in the case of kinematic branching, the values of the branching angle should be mainly determined by the structure of the strain field [19]. The agreement of the values of the branching angle obtained in this work with the theoretical value obtained from an analysis of the strain field under the principle of local symmetry [19] is quite remarkable. A direct assessment of the principle of local symmetry in our simulations would be very desirable. However, such an assessment is difficult to perform. First the branched cracks do not follow lattice directions and the nodes that get disconnected are not aligned, creating an alternating pattern that could be misinterpreted as a mode-II component. Second, the presence of sound waves generated by the disconnection events strongly perturbs the strain field near the tips.

VII. CONCLUSIONS

In this work we have reported the results of a series of simulations of a crack propagating through a discrete model of a brittle elastic solid. We show that, when the fracture criterion is implemented over nodes, instead of over bonds, the symmetry properties of the overall crack dynamics improve considerably. The implementation of the fracture criterion that we use here is the simplest one, but it fully avoids the possibility of mode-II perturbations. As a consequence the influence of the lattice directions on crack tip motion is dramatically reduced.

We have conducted a series of simulations to study the effect of notch length on the crack dynamics. Two kinds of behavior appear. Short-notch cases show strain fields with relatively small strain differences across the plate, which makes them highly sensitive to wave motion (and disorder, presumably), giving rise to highly branched patterns. On the

other hand, long-notch simulations show relatively high strain differences across the plate, giving smooth patterns. This happens because the crack dynamics becomes relatively insensitive to wave motion or disorder, unless the crack tip kinematics makes that γ_2^+ is slightly below γ_c^+.

During straight propagation the crack tip velocity shows an overall increasing trend with appreciable ripple. A close study to the crack tip acceleration shows strong oscillations that can be related to surface wave emission at the disconnection events.

Branching instabilities of two different types have been identified. In these simulations the first branching instability is due to the evolution of the strain field coupled to the crack tip motion. In the short-notch cases, the second branching instability can be unambiguously ascribed to the arrival to the crack tip of the surface wave pulse generated at the first disconnection event, reflected back at the upper boundary of the plate.

Finally, we also propose a qualitative kinematic model that allows for an explanation of the branching mechanism. The model considers a discrete elastic medium whose strain field would coincide with the corresponding plane strain field obtained from Yoffe's moving crack solution. Setting up a threshold value for disconnection in such a model is equivalent to consider that an "effective singularity" lags behind the crack tip a distance r_0 that is a model parameter. By analyzing the disconnection times of the nodes ahead and aside of the crack tip, we have shown that the evolution of the strain field, under a constant velocity motion of the effective singularity, can induce branching. Indeed, if the values of the model parameters are taken from appropriate fits to the simulation data, the critical tip velocity predicted agrees remarkably well with that found in the simulations. The analysis of the disconnection times might be a useful tool to understand the branching phenomenology in other discrete models of brittle fracture.

ACKNOWLEDGMENTS

We acknowledge fruitful discussions with S. Ciliberto, F. Guinea, E. Louis, A. Petri, and I. Zúñiga. This research has been supported by the Spanish M.C.Y.T. under Grant Nos. BFM2001-0290 and BFM2001-0297.

[1] T. A. Witten, Jr. and L. M. Sander, Phys. Rev. Lett. **47**, 1400 (1981).
[2] L. Niemeyer, L. Pietronero, and H. J. Wiesmannm, Phys. Rev. Lett. **52**, 1033 (1984).
[3] E. Louis and F. Guinea, Europhys. Lett. **3**, 871 (1987); R. Garciamolina, F. Guinea and E. Louis, Phys. Rev. Lett. **60**, 124 (1988).
[4] *Random Fluctuations and Pattern Growth: Experiments and Models*, edited by H. E. Stanley and N. Ostrowsky (Kluwer Academic, Dordrecht, 1988); *Statistical Models for the Fracture of Disordered Media*, edited by H. J. Herrmann and S. Roux (North-Holland, Amsterdam, 1990).
[5] L. B. Freund, *Dynamic Fracture Mechanics* (Cambridge University Press, New York, 1990).
[6] K. B. Broberg, *Cracks and Fracture* (Academic Press, San Diego, 1999).
[7] M. Elices, G. V. Guinea, J. Gómez, and J. Planas, Eng. Fract. Mech. **69**, 137 (2002); J. Planas, M. Elices, G. V. Guinea, F. J. Gómez, D. A. Cendón, and I. Arbilla, *ibid.* **70**, 1759 (2003); F. J. Gómez and M. Elices, *ibid.* **70**, 1913 (2003).
[8] J. Fineberg and M. Marder, Phys. Rep. **313**, 1 (1999).
[9] K. Ravi-Chandar and W. G. Knauss, Int. J. Fract. **25**, 247 (1984); **26**, 65 (1984); **26**, 141 (1984).
[10] J. Fineberg, S. P. Gross, M. Marder, and H. L. Swinney, Phys. Rev. Lett. **67**, 457 (1991).
[11] S. P. Gross, J. Fineberg, M. Marder, W. D. McCormick, and H. L. Swinney, Phys. Rev. Lett. **71**, 3162 (1993).
[12] J. F. Boudet, V. Steinberg, and S. Ciliberto, Europhys. Lett. **30**, 337 (1995); J. F. Boudet, S. Ciliberto and V. Steinberg, J. Phys. II **6**, 1493 (1996).
[13] J. F. Boudet and S. Ciliberto, Phys. Rev. Lett. **80**, 341 (1998); Physica D **142**, 317 (2000).
[14] E. Sharon, S. P. Gross, and J. Fineberg, Phys. Rev. Lett. **74**, 5096 (1995).
[15] S. Fratini, O. Pla, P. González, F. Guinea, and E. Louis, Phys. Rev. B **66**, 104104 (2002).
[16] A. Parisi and R. C. Ball, Phys. Rev. B **66**, 165432 (2002).
[17] E. H. Yoffe, Philos. Mag. **42**, 739 (1951).
[18] M. Adda-Bedia, R. Arias, M. Ben Amar, and F. Lund, Phys. Rev. Lett. **82**, 2318 (1999).
[19] M. Adda-Bedia, J. Mech. Phys. Solids **53**, 227 (2005).
[20] F. F. Abraham, Adv. Phys. **52**, 727 (2003).
[21] F. F. Abraham, D. Brodbeck, R. A. Rafey, and W. E. Rudge, Phys. Rev. Lett. **73**, 272 (1994); B. L. Hoolian and R. Ravelo, Phys. Rev. B **51**, 11 275 (1995); S. J. Zhou, P. S. Lomdahl, R. Thomson, and B. L. Holian, Phys. Rev. Lett. **76**, 2318 (1996); F. F. Abraham, *ibid.* **77**, 869 (1996); A. Omeltchenko, J. Yu, R. K. Kalia, and P. Vashishta, *ibid.* **78**, 2148 (1997); D. Holland and M. Marder, *ibid.* **80**, 746 (1998).
[22] J. Rottler, S. Barsky, and M. O. Robbins, Phys. Rev. Lett. **89**, 148304 (2002); J. Rottler and M. O. Robbins, *ibid.* **89**, 195501 (2002); , Phys. Rev. E **68**, 011801 (2003).
[23] X.-P. Xu and A. Needleman, J. Mech. Phys. Solids **42**, 1397 (1994).
[24] O. Pla, F. Guinea, E. Louis, S. V. Gaishas, and L. M. Sander, Phys. Rev. B **57**, R13 981 (1998). O. Pla, F. Guinea, E. Louis, S. V. Gaishas and L. M. Sander, Phys. Rev. B **61**, 11 472 (2000).
[25] T. Martín, P. Español, M. A. Rubio, and I. Zúñiga, Phys. Rev. E **61**, 6120 (2000).
[26] I. S. Aranson, V. A. Kalatsky, and V. M. Vinokur, Phys. Rev. Lett. **85**, 118 (2000).
[27] S. I. Heizler, D. A. Kessler, and H. Levine, Phys. Rev. E **66**, 016126 (2002).
[28] L. D. Landau and E. M. Lifshitz, *Theory of Elasticity* (Pergamon Press, New York, 1985).

[29] M. Born and K. Huang, *Dynamical Theory of Crystal Lattices* (Oxford University Press, London, 1954); H. Yan, G. Li, and L. M. Sander, Europhys. Lett. **10**, 7 (1989); G. Caldarelli, C. Castellano, and A. Vespignani, Phys. Rev. E **49**, 2673 (1994).
[30] Results on simulations with discretizations including next-nearest neighbours will be reported separately.
[31] M. P. Allen and D. J. Tildesley, *Computer Simulation of Liquids* (Clarendon Press, Oxford, 1987).
[32] Simulations performed with the fracture criterion in [25] allowing for surface recombination did not show any effect.
[33] This can be seen analytically for the case of the triangular notch (see, for instance, [6]) where as the notch gets shorter the singularity exponent decreases.
[34] W. G. Knauss, J. Appl. Mech. **33** 356 (1966).
[35] D. A. Kessler and H. Levine, Phys. Rev. E **68**, 036118 (2003).
[36] J. A. Hauch and M. P. Marder, Int. J. Heat Mass Transfer **90**, 133 (1998).
[37] I. Beery, U. Lev, and D. Sherman, J. Appl. Phys. **93**, 2429 (2003).
[38] The frequency domain analysis in Ref. [16] is not useful here because in this work the crack speed is not prescribed but a result of the dynamics.
[39] H. Henry and H. Levine, Phys. Rev. Lett. **93**, 105504 (2004).
[40] This analysis is valid also for a square lattice oriented at an angle of $\pi/4$ with respect to the plate boundaries just changing the terms by making $\theta_l = \pi/4$ and changing the unit term under the square root to the length of the unit cell diagonal, $\sqrt{(2)}$.
[41] A. J. Rosakis, C. Liu, and L. B. Freund, Int. J. Fract. **50**, R39 (1991).